Journal of Magnetic Resonance 198 (2009) 31–40

Contents lists available at ScienceDirect

Journal of Magnetic Resonance

journal homepage: www.elsevier.com/locate/jmr

3D Gradient coil design – toroidal surfaces

Peter T. While [a,*], Larry K. Forbes [a], Stuart Crozier [b]

[a] School of Mathematics & Physics, University of Tasmania, Private Bag 37, Hobart, Tasmania 7001, Australia
[b] School of Information Technology & Electrical Engineering, University of Queensland, St. Lucia, Brisbane, Qld 4072, Australia

ARTICLE INFO

Article history:
Received 4 September 2008
Revised 1 December 2008
Available online 19 January 2009

Keywords:
Magnetic resonance imaging (MRI)
Gradient coil design
Three-dimensional (3D) geometry
Inverse method
Torus
Toroidal

ABSTRACT

Gradient coil design typically involves optimisation of current densities or coil windings on familiar cylindrical, planar, spherical or conical surfaces. In this paper, an analytic inverse method is presented for the theoretical design of toroidal transverse gradient coils. This novel geometry is based on previous work involving a 3D current density solution, in which the precise geometry of the gradient coils was obtained as part of the optimisation process. Regularisation is used to solve for the toroidal current densities, whereby the field error is minimised in conjunction with the total power of the coil. The method is applied to the design of unshielded and shielded, whole-body and head coil gradient systems. Preliminary coil windings displaying high gradient homogeneity, low inductance, high efficiency and good force balancing are displayed and discussed. Potential benefits associated with this morphology include self-shielding gradient sets, greater access to cooling mechanisms, a reduction in acoustic noise due to force-balancing, a lessening of patient claustrophobia and greater patient access for clinicians.

1. Introduction

Magnetic resonance imaging (MRI) scanners contain gradient coils as a means of frequency-encoding the imaging volume. This is achieved by a set of three coils, which superimpose a linear magnetic field in each orthogonal direction, and are pulsed rapidly at specific times during image acquisition. Coil performance is governed by efficiency η, gradient homogeneity δ and inductance L [1]. Various combinations of these parameters are used as figures of merit [1–3].

Numerous coil-space optimisation techniques are available for the design of gradient coils, including conjugate gradient descent [4], simulated annealing [5] or the genetic algorithm (see for example, [6, p. 86]). An alternative branch of design methods deals with reciprocal space by expanding quantities of interest in terms of orthogonal functions and solving for the coefficients of a current density expansion [3]. A well-established example is Turner's target field method, in which a Fourier–Bessel expansion is used to describe the induced magnetic field and a current density solution is obtained using Fourier Transforms [7]. Typically this is achieved by minimising some feature of the coil such as inductance [8], stored magnetic energy [9] or power [10], subject to the constraint that the field be specified at a set of target points, following a Lagrange multiplier argument. The current density solution must then be approximated in some manner using discrete windings. This approach generally leads to more compact coils with less concentrated current, which results in increased efficiency and lower inductance [1].

A possible drawback of the target field method is that it assumes coils of notionally infinite length as a result of the use of Fourier Transforms. A Fourier series representation of the current density is proposed by Carlson et al. [2] to obtain a finite length coil, and coil length is constrained explicitly using a Turner-style target field method by Chronik and Rutt [3]. Forbes and Crozier [11] use a Fourier series expansion combined with Tikhonov regularisation (see for example, [12, p. 307]) to solve an ill-conditioned integral equation and obtain a finite length coil without approximation.

In addition to the standard primary design aim of arriving at an optimal trade-off between gradient homogeneity, coil efficiency and inductance (see also, [13]), many secondary concerns dictate design considerations for gradient coils. These include: the suppression of eddy currents via shielding (see for example, [14–16]); avoiding peripheral nerve stimulation (see for example, [17–19]); alleviating patient claustrophobia (see for example, [20]); and minimising acoustic noise caused by Lorentz forces (see for example, [21–24]).

In an attempt to address specific gradient problems further and improve coil performance, more recent gradient designs have tended to deviate away from the established primary plus shield coil, cylindrical or biplanar gradient system and a variety of geometries have been considered (see for example [25–33]). However, despite these methods being applicable and adaptable to arbitrary geometry, this geometry must still be chosen prior to the method being implemented. In contrast, a design method for whole-body transverse gradient coils is presented by While

* Corresponding author. Fax: +613 62262410.
E-mail address: pwhile@utas.edu.au (P.T. While).

1090-7807/$ - see front matter Crown Copyright © 2009 Published by Elsevier Inc. All rights reserved.
doi:10.1016/j.jmr.2009.01.006

et al. [34] that allows full freedom to explore arbitrary current distribution within 3D solution space. That is, the coil windings are not constrained to lie on some predetermined surface, but are instead found as part of the optimisation process. This method of gradient coil design can potentially offer a number of advantages. For example, integrated shielding may be possible, rather than having to consider separate surfaces for primary and shield coil windings. In addition, the resultant structures obtained may feature natural advantages in regards to cooling, force balancing and patient claustrophobia.

In While et al. [34], a 3D current density solution, contained within the volume between two coaxial cylinders of different radii, is obtained by minimising gradient field error in conjunction with total coil power using Tikhonov regularisation. Discrete 3D coil windings are obtained using a priority streamline technique and a secondary field optimisation for the coil currents, and these are found to display an interesting general geometric form involving sets of closed loops plus spiral-type coils. However, despite inducing an attractive magnetic field within the region of interest, coil efficiency is low due to the small number of windings and increasing this number results in an unattractive design in terms of manufacturability.

The aim of the present paper is to take the 3D gradient coil results of While et al. [34] and address the concerns of coil efficiency and manufacturability whilst maintaining the field accuracy and general geometry of the coil. The sets of closed loops plus spiral-type coils obtained in While et al. [34] are found to lie approximately on the surfaces of sets of elliptical tori. Therefore, using these 3D coil windings as a guide, we replace the 3D current density of While et al. [34] with a set of toroidal current density surfaces and repeat the gradient field optimisation. Provided field accuracy is maintained, this should yield gradient coil windings that are easy to manufacture via machine etching, and should also offer much greater freedom in regards to optimising the trade-off between coil efficiency, inductance and field error.

It is envisaged that further to this preliminary work, other gradient coil concerns, as mentioned previously, may be addressed using this 3D design method and similarly novel geometry. This method has the additional advantage of being semi-analytical in nature and avoids the computational constraints associated with the numerical techniques that dominate recent coil design.

The geometrical description of the toroidal surfaces will be presented in the following section. In Section 3, general forms for the components of this current density vector will be selected using Fourier series. A regularisation solution process will be outlined in Section 4, and the method for obtaining discrete coil windings from the continuous current density will be explained in Section 5, along with the means for calculating certain parameters measuring coil performance. Results will be displayed and compared in Section 6 for a variety of gradient coil designs, and some concluding remarks will be given in Section 7.

2. Elliptical tori and governing equations

Let us consider K elliptical tori of radius a_k $(k = 1 : K)$, with semi-major axes b_{k1} and semi-minor axes b_{k2}, lying coaxially with the z-axis and centred on the points $(x, y, z) = (0, 0, c_k)$. Fig. 1 illustrates this arrangement for the kth torus with cross-sections both in the (y, z) and (x, y) planes. Every point on the surface of the torus can be described using a position vector in terms of two coordinates, θ' and ϕ' (shown in Fig. 1), and this is given by:

$$\mathbf{r}'_k(\theta', \phi') = (a_k + b_{k2}\cos\phi')\cos\theta'\mathbf{e}_x + (a_k + b_{k2}\cos\phi')\sin\theta'\mathbf{e}_y + (c_k + b_{k1}\sin\phi')\mathbf{e}_z, \quad (1)$$

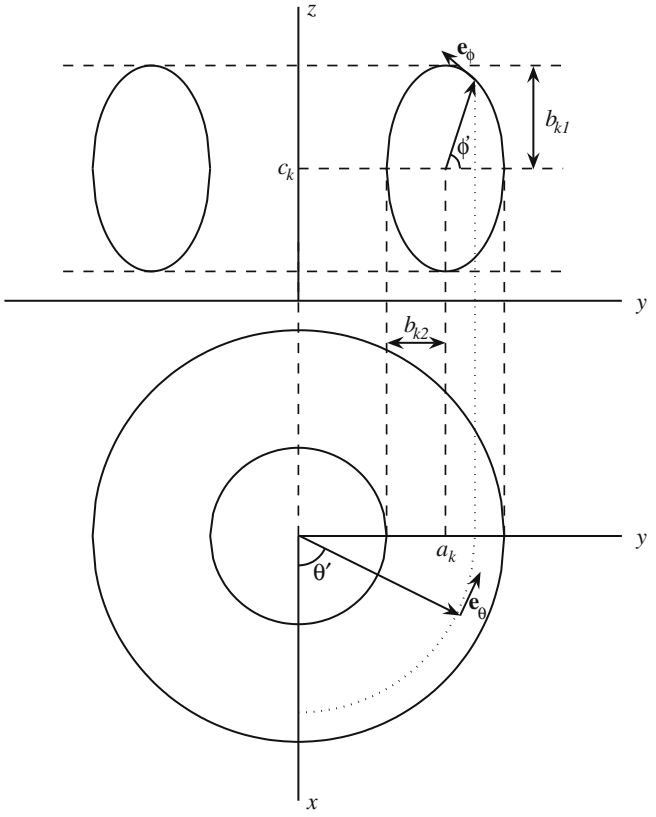

Fig. 1. The kth elliptical torus with radius a_k, semi-major axis b_{k1}, semi-minor axis b_{k2} and centred on the point $(x, y, z) = (0, 0, c_k)$. The top portion displays a cross-section in the (y, z) plane at $x = 0$ and shows the variable ϕ' and corresponding unit vector $\mathbf{e}_\phi$. The bottom portion displays a cross-section in the (x, y) plane at $z = c_k$ and shows the variable θ' and corresponding unit vector $\mathbf{e}_\theta$.

where the unit vectors $\mathbf{e}_x, \mathbf{e}_y$ and $\mathbf{e}_z$ point along the usual Cartesian x, y and z axes, respectively (see Fig. 1). We may also define the unit vectors:

$$\mathbf{e}_\theta = -\sin\theta'\mathbf{e}_x + \cos\theta'\mathbf{e}_y \quad (2)$$

$$\mathbf{e}_\phi = \frac{1}{\sqrt{b_{k1}^2\cos^2\phi' + b_{k2}^2\sin^2\phi'}} \times (-b_{k2}\sin\phi'\cos\theta'\mathbf{e}_x - b_{k2}\sin\phi'\sin\theta'\mathbf{e}_y + b_{k1}\cos\phi'\mathbf{e}_z), \quad (3)$$

and the scale functions:

$$h_{k\theta} = a_k + b_{k2}\cos\phi' \quad (4)$$

$$h_{k\phi} = \sqrt{b_{k1}^2\cos^2\phi' + b_{k2}^2\sin^2\phi'}, \quad (5)$$

for this orthogonal curvilinear coordinate system. Suppose some current density vector $\mathbf{j}_k(\mathbf{r}'_k)$ exists on the surface of the kth torus, at a source point with position vector $\mathbf{r}'_k$. Using Eqs. (2)-(5), this may be expressed in component form as follows:

$$\begin{aligned}\mathbf{j}_k(\mathbf{r}'_k) &= j_{k\theta}(\mathbf{r}'_k)\mathbf{e}_\theta + j_{k\phi}(\mathbf{r}'_k)\mathbf{e}_\phi \\ &= -\left(j_{k\theta}(\mathbf{r}'_k)\sin\theta' + j_{k\phi}(\mathbf{r}'_k)\frac{b_{k2}}{h_{k\phi}}\sin\phi'\cos\theta'\right)\mathbf{e}_x \\ &\quad + \left(j_{k\theta}(\mathbf{r}'_k)\cos\theta' - j_{k\phi}(\mathbf{r}'_k)\frac{b_{k2}}{h_{k\phi}}\sin\phi'\sin\theta'\right)\mathbf{e}_y \\ &\quad + j_{k\phi}(\mathbf{r}'_k)\frac{b_{k1}}{h_{k\phi}}\cos\phi'\mathbf{e}_z. \end{aligned} \quad (6)$$

The magnetic induction vector $\mathbf{B}(\mathbf{r})$ at the field point $\mathbf{r}$, induced by a surface current density vector $\mathbf{j}(\mathbf{r}')$ existing at the source point $\mathbf{r}'$ on

the surface S', can be obtained from the Biot-Savart law and is given by:

$$\mathbf{B}(\mathbf{r}) = \frac{\mu_0}{4\pi} \iint_{S'} \frac{(\mathbf{r}' - \mathbf{r}) \times \mathbf{j}(\mathbf{r}')}{\|\mathbf{r}' - \mathbf{r}\|^3} dA', \tag{7}$$

where μ_0 is the magnetic permeability of free-space. For the design of gradient coils, primary interest lies with the axial component of the magnetic induction vector, which for the present elliptical torus system can be expressed as follows:

$$B_z(x, y, z) = \frac{\mu_0}{4\pi} \sum_{k=1}^{K} \int_0^{2\pi}\int_0^{2\pi} \frac{1}{R_k^3} \{j_{k\theta}(h_{k\theta} - x\cos\theta' - y\sin\theta')h_{k\phi} + j_{k\phi}b_{k2}\sin\phi'(x\sin\theta' - y\cos\theta')\}h_{k\theta}d\theta' d\phi', \tag{8}$$

where

$$R_k = \{[h_{k\theta}\cos\theta' - x]^2 + [h_{k\theta}\sin\theta' - y]^2 + [(c_k + b_{k1}\sin\phi') - z]^2\}^{1/2}. \tag{9}$$

The aim is to solve for the current density components $j_{k\theta}$ and $j_{k\phi}$ $(k = 1 : K)$ such that the z-component of the induced magnetic field closely matches that of some desired target magnetic field over the surface of the DSV. This makes Eq. (8) a Fredholm integral equation of the first kind (see for example, [12, p. 299]) and is therefore likely to be ill-conditioned. However, a regularisation strategy will be discussed shortly to overcome this problem.

3. Toroidal current density and field expressions

The surface current density vector on each torus must have zero divergence, that is: $\nabla \cdot \mathbf{j}_k = 0$. Given the expression for $\mathbf{j}_k(\mathbf{r}'_k)$ in Eq. (6), the position vector $\mathbf{r}'_k$ for points on the kth torus given by Eq. (1), and the scale functions given by Eqs. (4) and (5), we have (see for example, [35, p. A64]):

$$\nabla \cdot \mathbf{j}_k = \frac{1}{h_{k\theta}h_{k\phi}} \left[\frac{\partial}{\partial\theta'}(j_{k\theta}h_{k\phi}) + \frac{\partial}{\partial\phi'}(j_{k\phi}h_{k\theta})\right]. \tag{10}$$

Eq. (10) can therefore be made zero by introducing a streamfunction $\psi_k(\theta', \phi')$ related to the components of the current density by means of the equations:

$$j_{k\theta}h_{k\phi} = \frac{\partial\psi_k}{\partial\phi'} \quad \text{and} \quad j_{k\phi}h_{k\theta} = -\frac{\partial\psi_k}{\partial\theta'}. \tag{11}$$

This means that we need only obtain the solution to one component of the current density. The streamfunction serves to be of further benefit as it can be shown that contours of $\psi_k(\theta', \phi')$ occur at equal intervals of current and hence give appropriate locations for coil windings (see for example, [36]).

Fourier series in terms of torus coordinates θ' and ϕ' are used to describe the components of the current density vector and the streamfunction:

$$\psi_k(\theta', \phi') = \sum_{m=1}^{M}\sum_{n=1}^{N}\{\cos n\phi'[A_{mnk}\cos m\theta' + B_{mnk}\sin m\theta'] + \sin n\phi'[C_{mnk}\cos m\theta' + D_{mnk}\sin m\theta']\} \tag{12}$$

$$j_{k\theta}(\theta', \phi') = \frac{-1}{h_{k\phi}} \sum_{m=1}^{M}\sum_{n=1}^{N} n\{\sin n\phi'[A_{mnk}\cos m\theta' + B_{mnk}\sin m\theta'] - \cos n\phi'[C_{mnk}\cos m\theta' + D_{mnk}\sin m\theta']\} \tag{13}$$

$$j_{k\phi}(\theta', \phi') = \frac{1}{h_{k\theta}} \sum_{m=1}^{M}\sum_{n=1}^{N} m\{\cos n\phi'[A_{mnk}\sin m\theta' - B_{mnk}\cos m\theta'] + \sin n\phi'[C_{mnk}\sin m\theta' + D_{mnk}\cos m\theta']\}. \tag{14}$$

Eqs. (12)-(14) involve four set of coefficients, A_{mnk}, B_{mnk}, C_{mnk} and $D_{mnk}(m = 1 : M, n = 1 : N, k = 1 : K)$, which are to be solved for later. Substituting Eqs. (13) and (14) into Eq. (8) and performing a change of variables $(\beta = \theta' - \theta)$, we express the axial component of the magnetic induction vector at any (r, θ, z) field point as follows:

$$B_z(r, \theta, z) = \mu_0 \sum_{k=1}^{K}\sum_{m=1}^{M}\sum_{n=1}^{N}\{U_{mnk}(r, z)[A_{mnk}\cos m\theta + B_{mnk}\sin m\theta] + V_{mnk}(r, z)[C_{mnk}\cos m\theta + D_{mnk}\sin m\theta]\}, \tag{15}$$

where for convenience we have introduced the intermediate functions:

$$U_{mnk}(r, z) = -\frac{1}{2\pi}\int_0^{2\pi}\int_0^{\pi} \frac{1}{R_k^3}[(h_{k\theta} - r\cos\beta)h_{k\theta}n\sin n\phi'\cos m\beta - b_{k2}rm\sin\phi'\sin\beta\cos n\phi'\sin m\beta]d\beta d\phi' \tag{16}$$

$$V_{mnk}(r, z) = \frac{1}{2\pi}\int_0^{2\pi}\int_0^{\pi} \frac{1}{R_k^3}[(h_{k\theta} - r\cos\beta)h_{k\theta}n\cos n\phi'\cos m\beta + b_{k2}rm\sin\phi'\sin\beta\sin n\phi'\sin m\beta]d\beta d\phi', \tag{17}$$

and

$$R_k = \left\{h_{k\theta}^2 - 2h_{k\theta}r\cos\beta + r^2 + [(c_k + b_{k1}\sin\phi') - z]^2\right\}^{1/2}. \tag{18}$$

That is, Eq. (15) gives the magnetic induction vector as a linear function of the unknown current density coefficients.

4. Regularisation solution process

The axial component of the magnetic induction vector (15) is required to match some desired target field on the surface of a spherical region of interest (DSV) with radius α and centred at the point $(x, y, z) = (0, 0, z_\alpha)$. Therefore, the following field error Φ_{DSV} is minimised with respect to the unknown coil coefficients:

$$\Phi_{DSV} = \alpha\int_{-\alpha+z_\alpha}^{\alpha+z_\alpha}\int_{-\pi}^{\pi}\{[B_z(r_\alpha, \theta, z) - B_{Tz}]^2\}d\theta dz, \tag{19}$$

where $r_\alpha = \sqrt{\alpha^2 - (z - z_\alpha)^2}$ and B_{Tz} is the z-component of the target field. For example, for the coefficient $A_{u\upsilon w}$ we have the condition:

$$\frac{\partial\Phi_{DSV}}{\partial A_{u\upsilon w}} = 2\pi\alpha\mu_0^2 \sum_{k=1}^{K}\sum_{n=1}^{N}\left\{A_{unk}\int_{-\alpha+z_\alpha}^{\alpha+z_\alpha} U_{unk}(r_\alpha, z)U_{u\upsilon w}(r_\alpha, z)dz + C_{unk}\int_{-\alpha+z_\alpha}^{\alpha+z_\alpha} V_{unk}(r_\alpha, z)U_{u\upsilon w}(r_\alpha, z)dz\right\} - 2\alpha\mu_0\int_{-\alpha+z_\alpha}^{\alpha+z_\alpha}\int_{-\pi}^{\pi} B_{Tz}(r_\alpha, \theta, z)U_{u\upsilon w}(r_\alpha, z)\cos u\theta d\theta dz = 0, \tag{20}$$

and similar conditions exist for the remaining three sets of coefficients.

Active shielding may be incorporated by minimising, in conjunction with Φ_{DSV} (19), the total magnetic flux Φ_S on the surface of some exterior cylindrical target region of length $2L$ and radius γ, centred about the origin:

$$\Phi_S = \gamma\int_{-L}^{L}\int_{-\pi}^{\pi} B_z^2(\gamma, \theta, z)d\theta dz. \tag{21}$$

For example, the shielding condition for coefficient $A_{u\upsilon w}$ is as follows:

$$\frac{\partial\Phi_S}{\partial A_{u\upsilon w}} = 2\pi\gamma\mu_0^2 \sum_{k=1}^{K}\sum_{n=1}^{N}\left\{A_{unk}\int_{-L}^{L} U_{unk}(\gamma, z)U_{u\upsilon w}(\gamma, z)dz + C_{unk}\int_{-L}^{L} V_{unk}(\gamma, z)U_{u\upsilon w}(\gamma, z)dz\right\}. \tag{22}$$

Therefore, to account for shielding, this condition (22) would be added to Eq. (20), along with similar expressions for the remaining sets of current density coefficients, and made equal to zero.

The integrals in Eqs. (20) and (22) may be evaluated numerically to obtain a system of linear equations in terms of the unknown current density Fourier coefficients, and the complete system can be expressed in matrix equation form:

$$(A + \lambda_S A_S)\mathbf{X} = \mathbf{T}. \tag{23}$$

Here matrix A (square) and vector $\mathbf{T}$ contain the field error conditions such as Eq. (20), matrix A_S (square) contains the shielding conditions such as Eq. (22), and the unknown coefficients are stored in vector $\mathbf{X}$ (length $4MNK$). A weighting λ_S has been applied to matrix A_S such that the shielding constraint may be scaled. As is typical of these kinds of problems, however, matrices A and A_S are found to be highly ill-conditioned and this can lead to gross errors in the corresponding solution.

A regularisation strategy is used to overcome this problem (see for example, [12, p. 307]), in which Φ_{DSV} (19) and Φ_S (21) are replaced by a residual error Γ, by adding a weighting λ_P of some additional constraint Π, before minimisation with respect to the coefficients:

$$\Gamma = \Phi_{\mathrm{DSV}} + \lambda_S \Phi_S + \lambda_P \Pi. \tag{24}$$

The regularising parameter λ_P behaves in a similar way to a Lagrange multiplier except that its value is left open for numerical experimentation. The choice of penalty function Π is largely up to the designer and in the present paper, as in While et al. [34], we choose Π to represent minimum power:

$$\Pi = \sum_{k=1}^{K} \int_{-\pi}^{\pi} \int_{-\pi}^{\pi} \left[j_{k\theta}^2 + j_{k\phi}^2 \right] h_{k\theta} h_{k\phi} d\theta' d\phi'. \tag{25}$$

Minimising the residual error Γ (24) demands the differentiation of Π (25) with respect to the current density coefficients. For example, for the coefficient $A_{u\upsilon w}$ we get:

$$\begin{aligned}\frac{\partial \Pi}{\partial A_{u\upsilon w}} = 2\pi \sum_{n=1}^{N} \Bigg\{ & A_{unw} \left[n\upsilon \int_{-\pi}^{\pi} \frac{h_{w\theta}}{h_{w\phi}} \sin n\phi' \sin \upsilon\phi' d\phi' \right. \\ & \left. + u^2 \int_{-\pi}^{\pi} \frac{h_{w\phi}}{h_{w\theta}} \cos n\phi' \cos \upsilon\phi' d\phi' \right] \\ & - C_{unw} \left[n\upsilon \int_{-\pi}^{\pi} \frac{h_{w\theta}}{h_{w\phi}} \cos n\phi' \sin \upsilon\phi' d\phi' \right. \\ & \left. - u^2 \int_{-\pi}^{\pi} \frac{h_{w\phi}}{h_{w\theta}} \sin n\phi' \cos \upsilon\phi' d\phi' \right] \Bigg\},\end{aligned} \tag{26}$$

and similar expressions are obtained for the remaining three sets of coefficients. The full system of linear equations is expressed in matrix equation form:

$$(A + \lambda_S A_S + \lambda_P P)\mathbf{X} = \mathbf{T}, \tag{27}$$

where matrix P contains the minimum power conditions such as Eq. (26). Increasing λ_P improves the conditioning of the matrix equation (27); however, this also reduces the accuracy with which the induced field can be matched to the target field, for which λ_P must be small [11]. Solving Eq. (27) yields the current density coefficients stored in vector $\mathbf{X}$. These can be used in conjunction with Eqs. (12)-(14) for the surface current density and Eq. (8) or (15) for the axial component of the magnetic induction vector.

5. Coil winding discretisation

Coil properties such as gradient homogeneity, efficiency and inductance can only be calculated sensibly with respect to physical coil windings and hence a discretisation of the current density is required. Coil windings are obtained by contouring ψ_k (12). This can be achieved using the program MATLAB™, for example, provided care is taken in choosing appropriate contour levels and in preserving current flow direction when storing contour vertices.

For a discretised system of K tori, each containing W_k $(k = 1 : K)$ coil windings described by the Q_{wk} vertices $(x'_{kwq}, y'_{kwq}, z'_{kwq})$ $(q = 1 : Q_{wk})$, and carrying currents I_k, the magnetic induction vector (7) becomes:

$$\mathbf{B}(\mathbf{r}) = \frac{\mu_0}{4\pi} \sum_{k=1}^{K} I_k \sum_{w=1}^{W_k} \sum_{q=1}^{Q_{wk}} \frac{(\mathbf{r}'_{kwq} - \mathbf{r}) \times \Delta \mathbf{s}'_{kwq}}{R_{kwq}^3}, \tag{28}$$

where

$$R_{kwq} = \left[(x'_{kwq} - x)^2 + (y'_{kwq} - y)^2 + (z'_{kwq} - z)^2 \right]^{1/2}. \tag{29}$$

Here vector $\mathbf{r}'_{kwq}$ describes the position vector for each coil winding vertex and vector $\mathbf{r}$ represents all field points of interest. Vector $\Delta \mathbf{s}'_{kwq}$ represents a discretised segment of the coil winding:

$$\Delta \mathbf{s}'_{kwq} = \Delta x'_{kwq} \mathbf{e}_x + \Delta y'_{kwq} \mathbf{e}_y + \Delta z'_{kwq} \mathbf{e}_z, \tag{30}$$

where, for example: $\Delta x'_{kwq} = x'_{kw,q+1} - x'_{kwq}$. The axial component of the magnetic induction vector is therefore given by:

$$B_z(x, y, z) = \frac{\mu_0}{4\pi} \sum_{k=1}^{K} I_k \sum_{w=1}^{W_k} \sum_{q=1}^{Q_{wk}} \frac{1}{R_{kwq}^3} \left[(x'_{kwq} - x) \Delta y'_{kwq} - (y'_{kwq} - y) \Delta x'_{kwq} \right]. \tag{31}$$

The greater the number of coil windings, the more accurately the field induced by the discretised system, given by Eq. (31), will match that of the continuous system given by Eq. (8) or (15).

Coil efficiency is calculated by taking the ratio of the gradient strength to coil current magnitude:

$$\eta = \frac{G}{max(I_k)} \qquad (\forall k = 1 : K). \tag{32}$$

Efficiency can be improved by increasing the number of coil windings. However, this can also increase coil inductance, which is undesirable.

Coil inductance for a volumetric current density $\mathbf{J}(\mathbf{r})$ may be calculated as follows (see for example, [6, p. 58]):

$$L = \frac{\mu_0}{4\pi I^2} \iiint_V \iiint_V \frac{\mathbf{J}(\mathbf{r}) \cdot \mathbf{J}(\mathbf{r}')}{\|\mathbf{r} - \mathbf{r}'\|} dv' dv, \tag{33}$$

where V denotes the volume of the conductor. For the discrete system this becomes:

$$\begin{aligned} L = \frac{\mu_0}{4\pi} \sum_{k=1}^{K} \sum_{h=1}^{K} \sum_{w=1}^{W_k} \sum_{v=1}^{W_h} \sum_{q=1}^{Q_{wk}} \sum_{p=1}^{Q_{vh}} \frac{1}{R_{khwvqp}} & \left[(x_{hv,p+1} - x_{hvp})(x_{kw,q+1} - x_{kwq}) \right. \\ & \left. + (y_{hv,p+1} - y_{hvp})(y_{kw,q+1} - y_{kwq}) + (z_{hv,p+1} - z_{hvp})(z_{kw,q+1} - z_{kwq}) \right], \end{aligned} \tag{34}$$

where

$$R_{khwvqp} = \left[(x_{hvp} - x_{kwq})^2 + (y_{hvp} - y_{kwq})^2 + (z_{hvp} - z_{kwq})^2 \right]^{1/2}. \tag{35}$$

Note that care must be taken to avoid any numerical errors caused by small or vanishing denominators.

Gradient homogeneity δ provides a means of quantitatively measuring the accuracy with which the induced field matches the target field and can be calculated as follows [1]:

$$\begin{aligned}\delta &= \frac{1}{V} \iiint_V \left[\frac{B_z(\mathbf{r}) - B_{Tz}}{B_{Tz}} \right]^2 dV \\ &= \frac{3}{4\pi\alpha^3} \int_{-\alpha+z_z}^{\alpha+z_z} \int_0^{2\pi} \int_0^{\sqrt{\alpha^2 - (z - z_z)^2}} \left[\frac{B_z(r, \theta, z) - B_{Tz}}{B_{Tz}} \right]^2 r dr d\theta dz,\end{aligned} \tag{36}$$

where the volume of integration is the DSV. The value $\sqrt{\delta}$ effectively gives a measure of total field error $\left(\sqrt{\delta}\times 100\%\right)$ over the volume of the DSV.

We may also estimate the Lorentz forces placed on the coil windings and the associated torque of the system. Lorentz forces arise as a result of the strong gradient currents being immersed in the powerful magnetic field induced by the main magnet. The switching of the gradient coils in this field subsequently establishes a pressure wave, which manifests as acoustic noise (see for example, [21]). The Lorentz force $\Delta\mathbf{F}$ acting on a wire segment $\Delta\mathbf{s}'$ (30) carrying current I within a magnetic field $\mathbf{B}$ is given by:

$$\Delta\mathbf{F} = I\Delta\mathbf{s}'\times\mathbf{B}. \tag{37}$$

If we assume that the magnetic field has a dominant z-component, B_{0z}, the x- and y-components of the total force on the system are given by:

$$F_x = B_{0z}\sum_{k=1}^{K} I_k \sum_{w=1}^{W_k}\sum_{q=1}^{Q_{wk}} (y'_{kw,q+1} - y'_{kwq}) \tag{38}$$

$$F_y = -B_{0z}\sum_{k=1}^{K} I_k \sum_{w=1}^{W_k}\sum_{q=1}^{Q_{wk}} (x'_{kw,q+1} - x'_{kwq}). \tag{39}$$

Eqs. (38) and (39) may be modified to consider the forces on individual tori or specific regions of the coil system.

The associated torque $\Delta\boldsymbol{\tau}$ on the winding segment $\Delta\mathbf{s}'$ in Eq. (37) is given by:

$$\Delta\boldsymbol{\tau} = \mathbf{r}'\times\Delta\mathbf{F}, \tag{40}$$

where $\mathbf{r}'$ is the position vector of the winding segment relative to some appropriate reference point. It is important that the torque be as small as possible to minimise coil deformation and ensure structural integrity (see for example, [25,13,26]). For the present toroidal gradient coil system, the components of the total torque vector are given by:

$$\tau_x = B_{0z}\sum_{k=1}^{K} I_k \sum_{w=1}^{W_k}\sum_{q=1}^{Q_{wk}} (x'_{kw,q+1} - x'_{kwq})(z'_{kwq} - z_0) \tag{41}$$

$$\tau_y = B_{0z}\sum_{k=1}^{K} I_k \sum_{w=1}^{W_k}\sum_{q=1}^{Q_{wk}} (y'_{kw,q+1} - y'_{kwq})(z'_{kwq} - z_0) \tag{42}$$

$$\tau_z = -B_{0z}\sum_{k=1}^{K} I_k \sum_{w=1}^{W_k}\sum_{q=1}^{Q_{wk}} [(x'_{kw,q+1} - x'_{kwq})(x'_{kwq} - x_0) + (y'_{kw,q+1} - y'_{kwq})(y'_{kwq} - y_0)], \tag{43}$$

where (x_0, y_0, z_0) is taken to be some reference point such as the origin or the centre of mass of the system.

6. Results and discussion

The results of While et al. [34] were used to guide the choice of geometrical parameters (see Fig. 1) and the number of tori considered. In that paper, the greatest success was achieved for an unshielded whole-body system comprising six sets of closed loops and spiral-type coil windings. This result is reshown here in Fig. 2. Therefore, we consider $K = 6$ tori and obtain parameters $(a_k, b_{k1}, b_{k2}, c_k)$ for each torus by mapping the vertices of the windings in Fig. 2 to the (r, z) plane and finding the best-fit elliptical cross-sections following a least squares type argument. Results for the first three tori are illustrated in Fig. 3 and parameter values for all six tori are summarised in Table 1.

A symmetrically located DSV was selected, as in While et al. [34], centred at the origin and with radius $\alpha = 0.15$ m. The target field was chosen to represent an x-gradient with gradient strength 50 mT/m, such that $B_{Tz} = 50\times 10^{-3} r_\alpha\cos\theta$ in Eq. (19), with

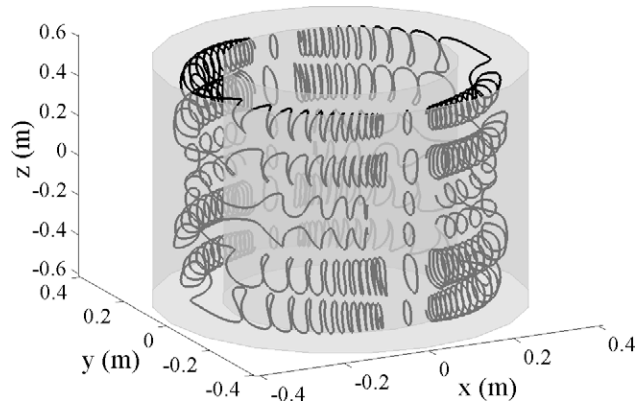

Fig. 2. The 24 coil windings used to approximate the 3D current density $\mathbf{J}(r', \theta', z')$ obtained for an unshielded x-gradient coil in While et al. [34].

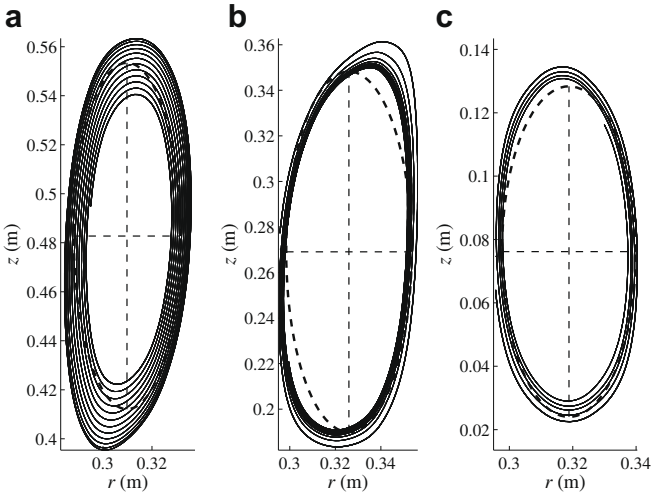

Fig. 3. The coil windings of Fig. 2 mapped to the (r, z) plane. The dashed lines represent cross-sections in this plane of the best-fit ellipses for the (a) first, (b) second, and (c) third torus.

$r_\alpha = \sqrt{\alpha^2 - (z - z_\alpha)^2}$. The outer cylindrical shielding target region was chosen to have length $2L = 1.2$ m, radius $\gamma = 0.6$ m and to be centred about the origin. The program MATLAB™ was used for numerical integration, for solving the matrix equations, and for plotting coil and field properties of interest. Numerical integration was performed over 20 intervals and the series representations for the current density components, given by Eqs. (13) and (14), were taken to $M = N = 11$ terms.

Results were obtained firstly for an unshielded transverse whole-body gradient system. That is, matrix A_S in Eq. (27) was ignored in solving for vector $\mathbf{X}$. The condition number of matrix A alone was found to be very high and of the order 10^{39}. Using a regularising parameter of $\lambda_P = 10^{-18}$, the condition number was decreased to the order 10^4, which allowed accurate solutions to be

Table 1
Parameter values (m) for the six tori of the whole-body gradient coil.

	Torus 1	Torus 2	Torus 3	Torus 4	Torus 5	Torus 6
a_k	0.3098	0.3260	0.3188	0.3188	0.3260	0.3098
c_k	0.4828	0.2691	0.0762	−0.0762	−0.2691	−0.4828
b_{k2}	0.0217	0.0275	0.0211	0.0211	0.0275	0.0217
b_{k1}	0.0707	0.0792	0.0522	0.0522	0.0792	0.0707

obtained. In conjunction with the aim of obtaining a well conditioned matrix system (27), the field error $\sqrt{\delta}$ (from Eq. (36)) associated with the continuous current density guided the choice of regularising parameter as it represented a limit to the field error attainable for the discretised system of coil windings. For the continuous current density result with $\lambda_P = 10^{-18}$ we find $\sqrt{\delta} = 0.0156$. That is, the field error over the volume of the DSV is approximately 1.56%.

When discretising the current density, by taking contours of the streamfunction ψ_k (12), a sufficiently large mesh of size 501×501 was considered to ensure convergence of all properties of interest. These contours were taken such that each winding on the same torus carried identical current, and windings on different tori carried as close to identical current as possible, limited only by the integer number of coil windings. The maximum current amongst the windings of all the tori was used in efficiency calculations, as dictated by Eq. (32). In practice, the small differences in coil current between tori may be achieved by the addition of a parallel resistor to each torus, however this is not ideal due to possible thermal instability. Alternatively, a preferred method is to adjust the streamfunction through the introduction of delta functions, as explained by Carlson et al. [2], to obtain an even current step.

As a first example, Fig. 4a displays a set of 128 coil windings obtained for the six tori of the unshielded transverse whole-body case with $\lambda_P = 10^{-18}$. Current is concentrated in the second and fifth torus; however this depends largely on the value of λ_P. Fig. 4b shows the winding pattern for the first torus plotted on the (θ, ϕ) plane (see Fig. 1) and displays a familiar fingerprint type pattern. On first look, the windings shown in Fig. 4a do not appear to resemble the spiral-type windings obtained in the 3D gradient work of While et al. [34], shown in Fig. 2. However, certain features are similar in a general sense. For example, in the portion of the coils in Fig. 2 where the spirals are tightly wound there is strong axial current, which is also observed in the same portion of the coils in Fig. 4a. Similarly, in the portion of the coils in Fig. 2 where the spirals open up (near the plane $y = 0$) there is strong azimuthal current, which is also observed in the same portion of the coils in Fig. 4a.

The axial component of the magnetic induction vector (31), corresponding to the coil windings in Fig. 4, is shown in Fig. 5 as a contour plot on the (r, z) plane at constant $\theta = 0$. The curved dashed line indicates the boundary of the DSV in this plane and an excellent match to the target field is observed within this region. This is confirmed by calculating the field error using Eq. (36), for which we find $\sqrt{\delta} = 0.0178$ (1.78%). Note that this value is only slightly larger than that found above for the continuous current density solution ($\sqrt{\delta} = 0.0156$). Alternatively, this corresponds to a 5% field error DSV of radius 0.202 m.

The maximum coil current is found to be 743 A, which for a gradient strength of 50 mT/m relates to a coil efficiency (32) of $\eta = 67.4$ μT/A/m. The inductance (34) for the present whole-body example is found to be $L = 634$ μH. Chronik and Rutt [3] introduce a figure of merit for measuring coil perfomance that is independent of the number of coil windings and coil radius a, given by $\eta a^{2.5}/\sqrt{L}$. For this first example we obtain the value $\eta a^{2.5}/\sqrt{L} = 1.53 \times 10^{-4}(\mathrm{Tm/A})^{1/2}$. In addition, we find that the field maximum on the exterior target region is 2.6 mT.

Coil efficiency can be improved by increasing the number of windings. However, this could present manufacturing difficulties and would also increase coil inductance One alternative may be to increase λ_P, which will reduce the power in the coil at the expense of gradient homogeneity and should lead to an improvement in efficiency for the same number of coil windings.

For example, for $\lambda_P = 10^{-17}$ a slightly improved efficiency of $\eta = 71.4$ μT/A/m was obtained for a reduced number of 108 coil windings. This reduction in coil windings, in conjunction with their smoother nature as λ_P is increased, also led to a reduced inductance of $L = 454$ μH and the value $\eta a^{2.5}/\sqrt{L} = 1.91 \times 10^{-4}(\mathrm{Tm/A})^{1/2}$. This improvement in coil performance was at the expense of gradient homogeneity, for which $\sqrt{\delta} = 0.0382$ (compared to $\sqrt{\delta} = 0.0373$ for the continuous current density). This represents a 3.82% field error, or expressed alternatively, a 5% field error DSV of radius 0.169 m. Figures for this $\lambda_P = 10^{-17}$ case have not been shown in interests of space but are similar in general form to Figs. 4 and 5. The reduction in coil power also results in a reduced field maximum on the exterior target region of 2.3 mT. As a further whole-body example, if we increase the number of coil windings for the $\lambda_P = 10^{-17}$ case from 108 to 140, we get a solution with $\eta = 90.1$ μT/A/m and $L = 756$ μH, for the same $\eta a^{2.5}/\sqrt{L}$ and $\sqrt{\delta}$ values.

Shielding can be incorporated by reintroducing the function Φ_S (21) into the residual error Γ (24), before minimising with respect to the current density coefficients. That is, conditions such as Eq. (22) are used to create matrix A_S in Eq. (27) before solving for

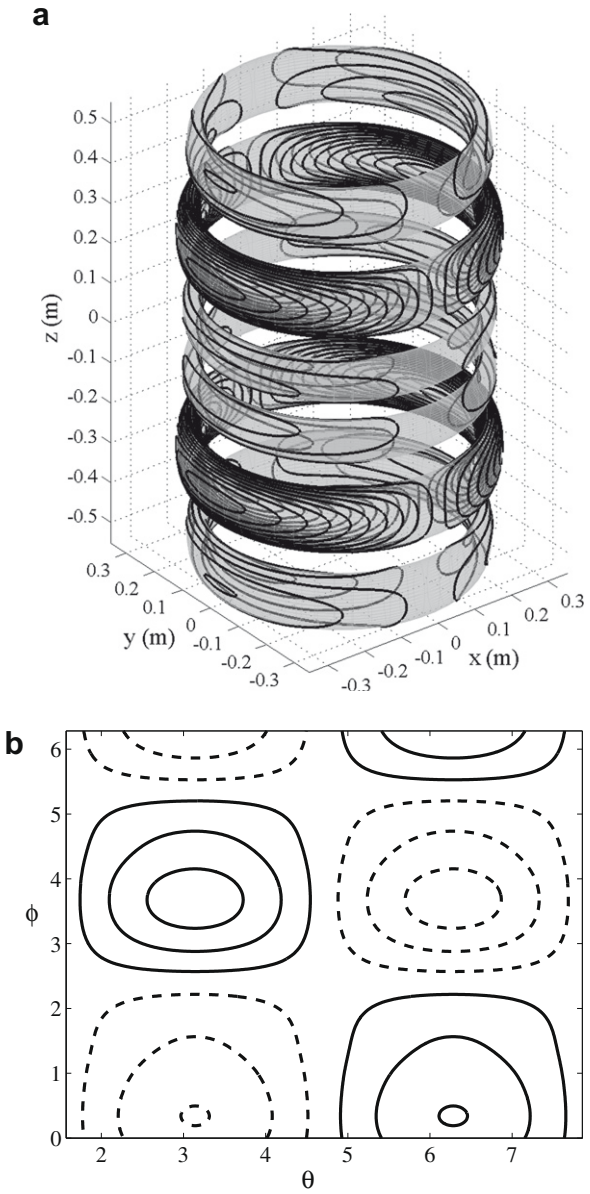

Fig. 4. (a) The 128 coil windings used to approximate the toroidal current densities $\mathbf{j}_k(\theta', \phi')$ $(k = 1 : K)$ for the six tori of the transverse whole-body case with $\lambda_P = 10^{-18}$. (b) The coil windings of the first torus in (a), plotted on the (θ, ϕ) plane, where the dashed lines represent reverse current in those portions of the coil.

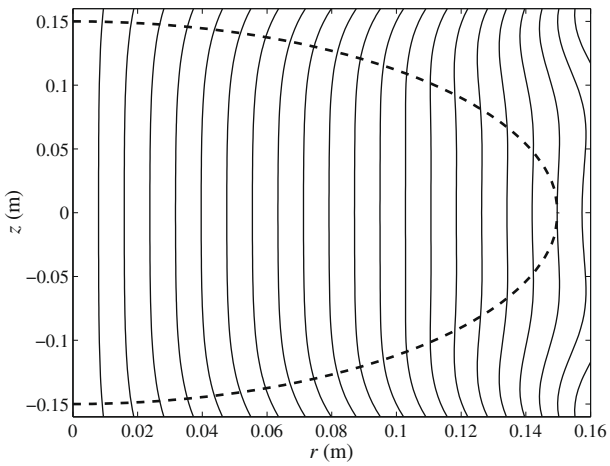

Fig. 5. Contour plot of the $B_z(r, \theta, z)$ field on the (r, z) plane $\theta = 0$, induced by the 128 coil windings of the whole-body coil illustrated in Fig. 4a. The curved dashed line represents the boundary of the DSV in this plane.

the coefficient vector **X**. For example, solving Eq. (27) with $\lambda_S = 1$ and $\lambda_P = 10^{-18}$ and discretising the current density with 204 coil windings, gives a shielded gradient system displaying an efficiency $\eta = 49.7\ \mu T/A/m$, an inductance $L = 473\ \mu H \left(\eta a^{2.5}/\sqrt{L} = 1.30 \times 10^{-4} (Tm/A)^{1/2}\right)$ and a field error $\sqrt{\delta} = 0.0488$ (4.88%). This represents approximately a 70% reduction in coil performance, which is typical for shielded gradients. The field maximum on the exterior target region is found to be 0.12 mT and represents a 95% improvement when compared to the unshielded design. Figures have not been shown in interests of brevity, however this example demonstrates that it is possible to incorporate active self-shielding successfully into the present gradient coil design methodology.

The Lorentz forces acting on the gradient coils can be calculated using Eqs. (38) and (39) and for the whole-body examples considered above are found to be of the order 10^{-11}—10^{-15} N. This is despite the sum of the magnitudes of the forces being of the order 10^4—10^5 N. However, it is important to modify Eqs. (38) and (39) to calculate the net force over the two halves of the system, $x > 0$ and $x < 0$ (see for example, Fig. 4a), for each torus, thus isolating individual sets of coil windings. These net forces are all found to be very small and of the order 10^{-11}—10^{-14} N. Therefore, these preliminary results suggest that considerable force cancelling is achieved with these toroidal whole-body gradient coil designs.

The associated torque may be calculated using Eqs. (41)-(43). For all the above whole-body examples, the x- and y-components of the torque, τ_x and τ_y, were found to be negligible and of the order 10^{-10}—10^{-14} Nm. This is very small when compared to other gradient coil designs (see for example, [25]), particularly considering that torque has not been minimised directly as part of the optimisation process. The z-component of the torque, τ_z, is much larger with magnitude approximately equal to 150 Nm for the above unshielded examples (twice this for the shielded example), which relates to an azimuthal twisting of the coil about the z-axis. This corresponds to a torque per unit current per unit field strength of around 0.2–0.3 Nm/A/T, which is appropriate for systems without direct torque balancing (see for example, [13]).

The figure of merit $\eta a^{2.5}/\sqrt{L}$ was calculated for a wide variety of contemporary unshielded and shielded whole-body transverse gradient coil designs, such that the preliminary results presented thus far could be compared in terms of coil performance. A considerable spread of values were obtained and typically fell in the range $\eta a^{2.5}/\sqrt{L} = 0.85$—$2.2 \times 10^{-4} (Tm/A)^{1/2}$ for recent whole-body designs [3,25,30,18,19]. Recall that the toroidal unshielded coil has $\eta a^{2.5}/\sqrt{L} = 1.91 \times 10^{-4} (Tm/A)^{1/2}$ and the shielded coil $\eta a^{2.5}/\sqrt{L} = 1.30 \times 10^{-4} (Tm/A)^{1/2}$, which are therefore both competitive with modern designs. However, it is important to stress that many other design criteria must be considered in any direct comparison betwen coils. For instance, the toroidal designs presented here display a large linear field region and considerable force cancelling characteristics. In addition, the unique geometry and novel design method show promise for optimising additional design criteria in subsequent work.

Other dedicated coil types can be considered in a straightforward manner using the present design methodology, simply by altering the geometric parameters defining each torus. For example, a dome-like head coil structure was considered such that windings could be placed as close to the head, and hence the DSV, as possible (see for example, [25,31,32]). The parameters for the whole-body case, given in Table 1, were used as a guide in maintaining semi-major to semi-minor axis ratios for the ellipses. However to fit the structure of the coil best, these ratios were skewed by a function of torus position around the dome. In addition, to obtain better coverage of the coil volume, gap sizes between adjacent tori were reduced for this head coil example. This approach was investigated for reasons of immediacy and convenience, rather than resolving for a 3D current density as in While et al. [34]. The chosen structure for the head coil is illustrated in Fig. 6 and the geometric parameter values for all six tori are summarised in Table 2.

A smaller DSV of radius $a = 0.075$ m was chosen, centred at the point $(x, y, z) = (0, 0, z_\alpha)$, with $z_\alpha = 0.15$ m (dashed line in Fig. 6). The target field was chosen to represent an x-gradient with gradient strength 50 mT/m; however, shielding was not considered for this coil design. Choosing $\lambda_P = 10^{-22}$ reduced the condition number of the matrix equation (27) from the order of 10^{32} to 10^9, such that accurate solutions could be obtained. The corresponding continuous current density solution induced a field with error

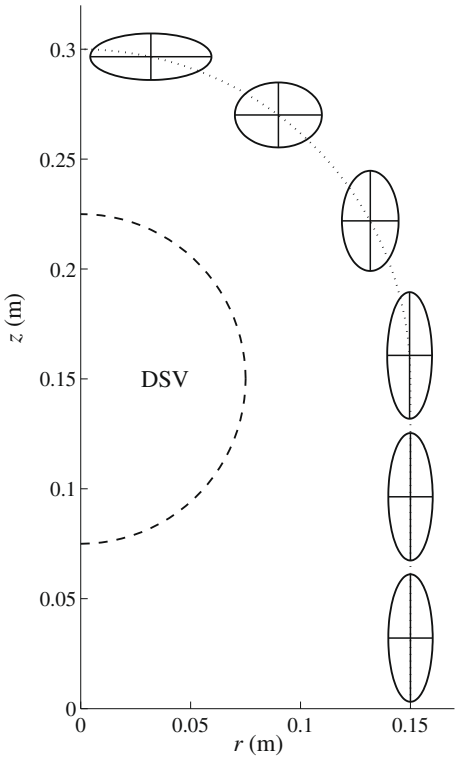

Fig. 6. Cross-section in the (r, z) plane of the six elliptical tori used in the transverse head coil design. The dotted line represents the cylinder plus hemisphere dome-like structure and the dashed line represents the boundary of the DSV in this plane.

Table 2
Parameter values (m) for the six tori of the head gradient coil.

	Torus 1	Torus 2	Torus 3	Torus 4	Torus 5	Torus 6
a_k	0.0319	0.0899	0.1317	0.1496	0.1500	0.1500
c_k	0.2966	0.2701	0.2219	0.1607	0.0964	0.0321
b_{k2}	0.0276	0.0198	0.0129	0.0102	0.0101	0.0101
b_{k1}	0.0106	0.0148	0.0228	0.0288	0.0290	0.0290

$\sqrt{\delta} = 0.0022$ (0.22%), which served as a limit for any discretised system of coil windings.

Fig. 7 displays a discretised set of 136 windings over the six tori of the present head coil example with $\lambda_P = 10^{-22}$. Note that the current is much more evenly spread amongst tori when compared to the whole-body coil of Fig. 4a. The maximum coil current has a value of 273 A, such that the efficiency is $\eta = 183.4$ μT/A/m, which is high. The inductance is calculated to be $L = 115$ μH, such that $\eta a^{2.5}/\sqrt{L} = 1.49 \times 10^{-4}(\mathrm{Tm/A})^{1/2}$. Fig. 8 displays a contour plot of the axial component of the induced field on the (r, z) plane, with $\theta = 0$. A highly linear field is induced within the DSV and the field error is found to be $\sqrt{\delta} = 0.0329$ (3.29%, or a 5% field error DSV of radius 0.102 m). Note, for comparison, that the field maximum on an exterior cylindrical target region of radius $\gamma = 0.25$ m and length $L = 0.35$ m is found to be 0.84 mT for this head coil example. Reducing the number of coil windings to 92 (instead of 136) results in an induced field with much the same field error but at a lower efficiency of $\eta = 123$ μT/A/m and with a lower inductance of $L = 53$ μH (same $\eta a^{2.5}/\sqrt{L}$).

As illustrated above with the whole-body system, the coil efficiency to inductance trade-off can be improved potentially by increasing the value of the regularising parameter λ_P. This reduces the power of the coil system and also smoothens the current density and hence the coil windings, and therefore can be beneficial to both efficiency and inductance. For example, Fig. 9 displays a discretised set of only 52 windings over the six tori of a head coil design with $\lambda_P = 5 \times 10^{-19}$. Despite the low number of coil windings, this coil was found to have an efficiency $\eta = 114.4$ μT/A/m and an inductance $L = 28$ μH, such that $\eta a^{2.5}/\sqrt{L} = 1.90 \times 10^{-4}(\mathrm{Tm/A})^{1/2}$, and a field error $\sqrt{\delta} = 0.0253$ (2.53%). That is, the efficiency–inductance trade-off is superior to the $\lambda_P = 10^{-22}$ example of Fig. 7 and the field error is actually smaller (although the 5% field error DSV has a smaller radius of 0.095 m). This demonstrates the nonlinear behaviour of λ_P when solving Eq. (27). A field plot has not been shown in interests of space but is similar to Fig. 8. Increasing the number of coil windings to 76 increases efficiency but also inductance, to $\eta = 160.2$ μT/A/m and $L = 58$ μH, respectively, $\left(\eta a^{2.5}/\sqrt{L} = 1.83 \times 10^{-4}(\mathrm{Tm/A})^{1/2}\right)$, for approximately the same field error. For both of these examples, the field maximum on the exterior target region is found to be 1.1 mT.

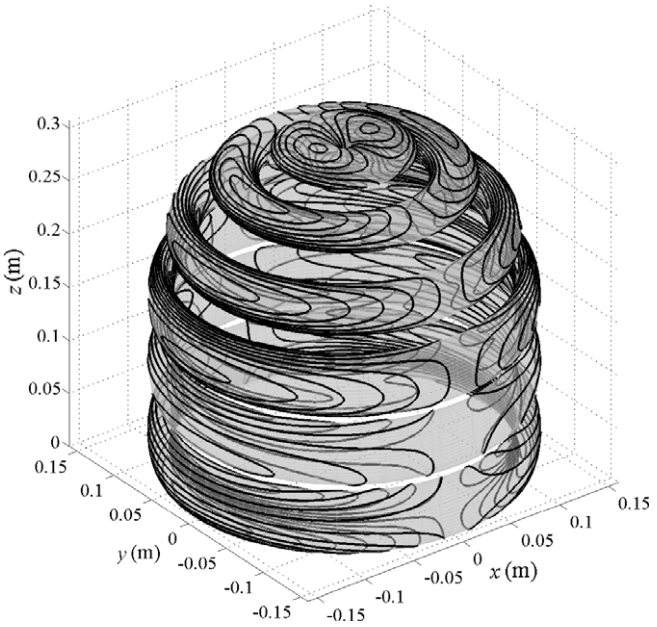

Fig. 7. The 136 coil windings used to approximate the toroidal current densities $\mathbf{j}_k(\theta', \phi')$ $(k = 1 : K)$ for the six tori of the transverse head coil case with $\lambda_P = 10^{-22}$.

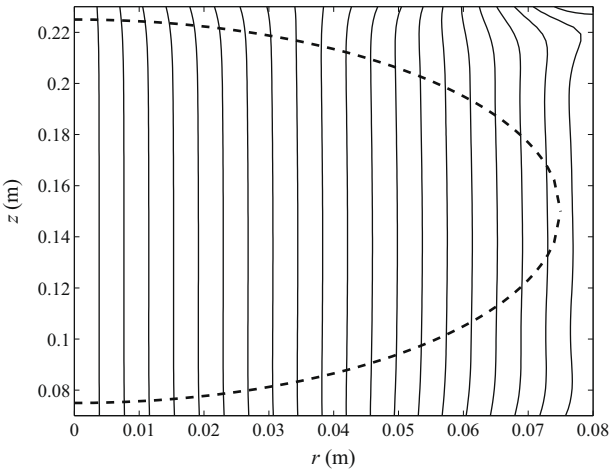

Fig. 8. Contour plot of the $B_z(r, \theta, z)$ field on the (r, z) plane $\theta = 0$, induced by the 136 coil windings of the head coil illustrated in Fig. 7. The curved dashed line represents the boundary of the DSV in this plane.

The sum of the Lorentz forces on the coil windings in each half, $x > 0$ and $x < 0$ (see for example, Fig. 9), of each torus of the above head coil examples is found to be negligible (order 10^{-12}—10^{-15} N), as was similarly found for the whole-body cases. This is despite the large individual magnitudes of the forces and again suggests that considerable force cancelling is achieved with these toroidal gradient coil designs. In contrast to the whole-body designs, however, the head coil designs have a dominant y-component of the torque vector. For the $\lambda_P = 10^{-22}$ cases, $\tau_y \approx -110$ Nm, $\tau_z \approx -11$ Nm and τ_x is negligible, such that the torque per unit current per unit field strength is about 0.3–0.4 Nm/A/T. For the $\lambda_P = 5 \times 10^{-19}$ cases, these quantities are smaller by a factor of about 4.

Presently it is unclear what dependence the results obtained thus far have on the precise geometry of the elliptical torus surfaces. To investigate this dependence, the elliptical tori of the head coil displayed in Fig. 6 were replaced with circular tori of equal cross-sectional area, and the model resolved for a number of comparable cases. That is, the parameters in Table 2 were used once more, except that all b_{k1} and b_{k2} values were replaced with $b_k = 0.0171$ m. As a direct comparison to the elliptical torus head coil displayed in Fig. 9, Eq. (27) was resolved for the circular torus head coil described above, with $\lambda_P = 5 \times 10^{-19}$, and the current density solution was discretised into 54 coil windings (as close to 52 as possible). This design was found to have an efficiency $\eta = 85$ μT/A/m and an inductance $L = 25$ μH, such that $\eta a^{2.5}/\sqrt{L} = 1.48 \times 10^{-4}(\mathrm{Tm/A})^{1/2}$, and a field error $\sqrt{\delta} = 0.0253$ (2.53%, or a 5% field error DSV of radius 0.097 m). This is an inferior coil design to the elliptical torus head coil of Fig. 9, for which $\eta a^{2.5}/\sqrt{L} = 1.90 \times 10^{-4}$ $(\mathrm{Tm/A})^{1/2}$, and provisionally suggests that the precise elliptic form of the torus cross-sections may be important in optimising results.

However, as a final example, discretising the circular torus head coil with 74 windings was found to increase the efficiency to $\eta = 152.8$ μT/A/m but increase the inductance only to $L = 45$ μH,

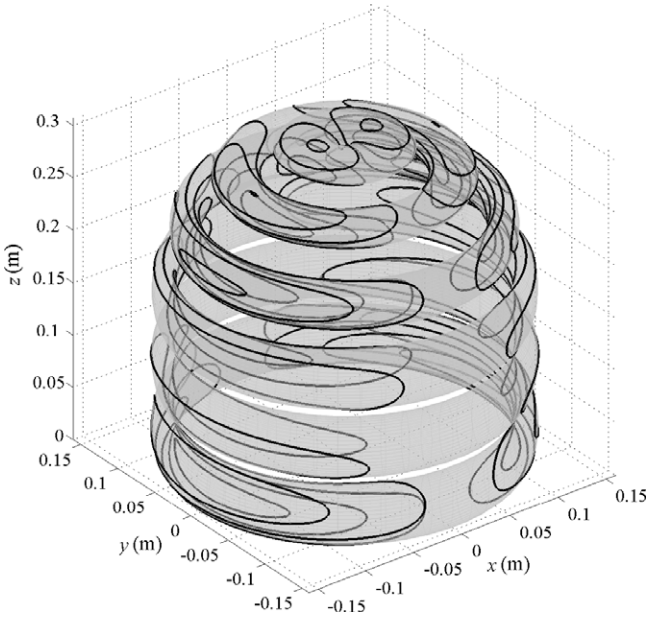

Fig. 9. The 52 coil windings used to approximate the toroidal current densities $\mathbf{j}_k(\theta', \phi')(k = 1 : K)$ for the six tori of the transverse head coil case with $\lambda_P = 5 \times 10^{-19}$.

such that $\eta a^{2.5}/\sqrt{L} = 1.99 \times 10^{-4}(\mathrm{Tm/A})^{1/2}$, for a field error of $\sqrt{\delta} = 0.0231$ (2.31%, or a 5% field error DSV of radius 0.098 m). That is, the efficiency–inductance trade-off for this circular torus design is apparently superior to that of the equivalent elliptical torus design described above (for which $\eta a^{2.5}/\sqrt{L} = 1.83 \times 10^{-4}(\mathrm{Tm/A})^{1/2}$). In addition, the field maximum on the exterior target region is found to be only 0.4 mT, which represents a 64% improvement over the elliptical torus head coil of Fig. 9, and the torque per unit current per unit field strength is slightly smaller. Note however, that in all these head coil examples we have not included active shielding, nor torque minimisation.

This final result still suggests that the precise torus geometry is important, but perhaps that the approximate values of Table 2 and the chosen elliptic form of Fig. 6 are not entirely optimal. A more indepth analysis would require the application of the 3D design method of While et al. [34] to a head gradient coil, however further fine-tuning of the torus geometry is beyond the scope of the present paper and will be left for future research. Note that the added advantage of using circular tori to construct the head coil is with regards to ease of manufacture, and this consideration may well outweigh any perceived benefits from fine-tuning the geometry further.

As a means of judging coil performance for the presented preliminary head coil designs, the figure of merit $\eta a^{2.5}/\sqrt{L}$ was calculated for a number of recently published transverse head gradients (and similar). A wide spread of values were obtained, with $\eta a^{2.5}/\sqrt{L} = 0.78\text{–}2.74 \times 10^{-4}(\mathrm{Tm/A})^{1/2}$ [25,31,32,18,26,22], which demonstrates the competitive quality of the toroidal head coils $\left(\eta a^{2.5}/\sqrt{L} = 1.99 \times 10^{-4}(\mathrm{Tm/A})^{1/2}\right)$. In addition, a superior level of gradient homogeneity is observed when compared to several of these contemporary designs and the coils have also been shown to display excellent force balancing.

7. Conclusion

An inverse method has been presented for the theoretical design of transverse gradient coils. The basic geometry of the gradient coil was chosen based on the results of While et al. [34]. Those authors considered a fully 3D current density and a priority streamline method to obtain coil windings that optimised the induced field subject to a minimum power constraint. Results from While et al. [34] involved sets of closed loops plus spiral-type coil windings and dictated the use of toroidal current density surfaces as the preferred geometry in the present paper.

A regularisation strategy was used to solve for the toroidal surface current densities. That is, the field error between the induced and linear target fields within the DSV was minimised along with a constraint representing the total power in the coil. The current density was then discretised, via a streamfunction method, to obtain individual coil windings on each torus.

Several unshielded and shielded, whole-body and head coil examples were considered. These highlighted the trade-off between gradient homogeneity, coil inductance and efficiency. In addition, it was demonstrated how varying the regularising parameter could improve coil performance. Coil windings displaying high efficiency, low inductance, high gradient homogeneity and good force balancing were obtained both for a cylindrical whole-body design and a dome-like head coil design. In addition, the elliptical torus structure was shown to display an inherent self-shielding property and hence a compact overall form.

Further optimisation of the precise geometry of the tori may yield even more attractive results. However, this must be balanced against the ease of manufacture of the gradient coil, such as that afforded by a circular torus design, for which excellent results are nevertheless still attainable.

In addition to the self-shielding property, the general structure of the system may potentially offer further advantages. For example, the gaps between (or spaces inside) the tori allow greater access for cooling mechanisms to improve thermal performance. These gaps may also allay patient claustrophobia concerns and afford improved patient access by allowing more open systems. Furthermore, the separately contained elements comprising the coil system have been shown in preliminary results to aid force balancing, which should serve to reduce acoustic noise generated by the coil.

The combined design method of While et al. [34] and the present paper allows considerable freedom in the optimisation of a wide range of design criteria. The utility of the third radial dimension can potentially lead to additional novel and interesting coil geometries to the toroidal structures presented in this paper. The method has the added advantage of being semi-analytical and hence fully tractable and computationally non-intensive. In light of the preliminary results presented here, further work will look at more direct treatment of gradient issues such as acoustic noise, peripheral nerve stimulation and thermal performance, using the present 3D design method.

References

[1] R. Turner, Gradient coil design: a review of methods, Magn. Reson. Imag. 11 (1993) 903–920.
[2] J.W. Carlson, K.A. Derby, K.C. Hawryszko, M. Weideman, Design and evaluation of shielded gradient coils, Magn. Reson. Med. 26 (1992) 191–206.
[3] B.A. Chronik, B.K. Rutt, Constrained length minimum inductance gradient coil design, Magn. Reson. Med. 39 (1998) 270–278.
[4] E.C. Wong, A. Jesmanowicz, J.S. Hyde, Coil optimization for MRI by conjugate gradient descent, Magn. Reson. Med. 21 (1991) 39–48.
[5] S. Crozier, L.K. Forbes, D.M. Doddrell, The design of transverse gradient coils of restricted length by simulated annealing, J. Magn. Reson. 107 (1994) 126–128.
[6] J. Jin, Electromagnetic Analysis and Design in Magnetic Resonance Imaging, CRC Press, Florida, 1999, pp. 21, 58, 86, 90.
[7] R. Turner, A target field approach to optimal coil design, J. Phys. D Appl. Phys. 19 (1986) L147–L151.
[8] R. Turner, Minimum inductance coils, J. Phys. E Sci. Instrum. 21 (10) (1988) 948–952.
[9] M.A. Martens, L.S. Petropoulos, R.W. Brown, J.H. Andrews, M.A. Morich, J.L. Patrick, Insertable biplanar gradient coils for magnetic resonance imaging, Rev. Sci. Instrum. 62 (11) (1991) 2639–2645.
[10] D.I. Hoult, R. Deslauriers, Accurate shim-coil design and magnet-field profiling by a power-minimization-matrix method, J. Magn. Reson. 108 (1994) 9–20.

[11] L.K. Forbes, S. Crozier, A novel target-field method for finite-length magnetic resonance shim coils: II. Tesseral shims, J. Phys. D Appl. Phys. 35 (2002) 839–849.
[12] L.M. Delves, J.L. Mohamed, Computational Methods for Integral Equations, Cambridge University Press, Cambridge, UK, 1985. 299–307.
[13] H. Sanchez, F. Liu, A. Trakic, S. Crozier, A simple relationship for high efficiency–gradient uniformity tradeoff in multilayer asymmetric gradient coils for magnetic resonance imaging, IEEE Trans. Magn. 43 (2) (2007) 523–532.
[14] L.K. Forbes, S. Crozier, A novel target-field method for finite-length magnetic resonance shim coils: III. Shielded zonal and tesseral coils, J. Phys. D Appl. Phys. 36 (2003) 68–80.
[15] A. Trakic, F. Liu, H. Sanchez-Lopez, H. Wang, S. Crozier, Longitudinal gradient coil optimization in the presence of transient eddy currents, Magn. Reson. Med. 57 (2007) 1119–1130.
[16] T.N. Baig, T.P. Eagan, L.S. Petropoulos, T.K. Kidane, W.A. Edelstein, R.W. Brown, Gradient coil with active endcap shielding, Concepts Magn. Reson. B Magn. Reson. Eng. 31B (2007) 12–23.
[17] A. Kangarlu, P.M.L. Robitaille, Biological effects and health implications in magnetic resonance imaging, Concepts Magn. Reson. 12 (5) (2000) 321–359.
[18] D.L. Parker, J.R. Hadley, Multiple-region gradient arrays for extended field of view, increased performance, and reduced nerve stimulation in magnetic resonance imaging, Magn. Reson. Med. 56 (2006) 1251–1260.
[19] R. Kimmlingen, M. Gebhardt, J. Schuster, M. Brand, F. Schmitt, A. Haase, Gradient system providing continuously variable field characteristics, Magn. Reson. Med. 47 (2002) 800–808.
[20] L.K. Forbes, M.A. Brideson, S. Crozier, A target-field method to design circular biplanar coils for asymmetric shim and gradient fields, IEEE Trans. Magn. 41 (6) (2005) 2134–2144.
[21] L.K. Forbes, M.A. Brideson, S. Crozier, P.T. While, An analytical approach to the design of quiet cylindrical asymmetric gradient coils in MRI, Concepts Magn. Reson. B Magn. Reson. Eng. 31B (4) (2007) 218–236.
[22] R. Bowtell, A. Peters, Analytic approach to the design of transverse gradient coils with co-axial return paths, Magn. Reson. Med. 41 (1999) 600–608.
[23] B.L.W. Chapman, P. Mansfield, Quiet gradient coils: active acoustically and magnetically screened distributed transverse gradient designs, Meas. Sci. Tech. 6 (1995) 349–354.
[24] N.B. Roozen, A.H. Koevoets, A.J. den Hamer, Active vibration control of gradient coils to reduce acoustic noise of MRI systems, IEEE/ASME Trans. Mechatron. 13 (3) (2008) 325–333.
[25] M. Poole, R. Bowtell, Novel gradient coils designed using a boundary element method, Concepts Magn. Reson. B Magn. Reson. Eng. 31B (3) (2007) 162–175.
[26] R.A. Lemdiasov, R. Ludwig, A stream function method for gradient coil design, Concepts Magn. Reson. B Magn. Reson. Eng. 26B (2005) 67–80.
[27] P. Mansfield, B. Haywood, Controlled E-field gradient coils for MRI, Phys. Med. Biol. 53 (7) (2008) 1811–1827.
[28] B. Haywood, B. Chapman, P. Mansfield, Model gradient coil employing active acoustic control for MRI, Magn. Reson. Mater. Phys. Biol. Med. 20 (5–6) (2007) 223–231.
[29] J. Leggett, S. Crozier, S. Blackband, B. Beck, R.W. Bowtell, Multilayer transverse gradient coil design, Concepts Magn. Reson. B Magn. Reson. Eng. 16B (2003) 38–46.
[30] S. Shvartsman, M. Morich, G. Demeester, Z. Zhai, Ultrashort shielded gradient coil design with 3D geometry, Concepts Magn. Reson. B Magn. Reson. Eng. 26B (2005) 1–15.
[31] H. Sanchez, F. Liu, A. Trakic, E. Weber, S. Crozier, Three-dimensional gradient coil structures for magnetic resonance imaging designed using fuzzy membership functions, IEEE Trans. Magn. 43 (9) (2007) 3558–3566.
[32] V. Vegh, H. Sanchez, I.M. Brereton, S. Crozier, Toward designing asymmetric head gradient coils for high-resolution imaging, Concepts Magn. Reson. B Magn. Reson. Eng. 31B (2007) 1–11.
[33] S. Shvartsman, M.C. Steckner, Discrete design method of transverse gradient coils for MRI, Concepts Magn. Reson. B Magn. Reson. Eng. 31B (2) (2007) 95–115.
[34] P.T. While, L.K. Forbes, S. Crozier, 3D gradient coil design—initial theoretical framework, IEEE Trans. Biomed. Eng. in press, 2009.
[35] E. Kreyszig, Advanced Engineering Mathematics, eighth ed., John Wiley & Sons, Inc., Singapore, 1999. p. A64.
[36] M.A. Brideson, L.K. Forbes, S. Crozier, Determining complicated winding patterns for shim coils using streamfunctions and the target-field method, Concepts Magn. Reson. 14 (2002) 9–18.